# Overall survival prediction in glioblastoma patients using structural magnetic resonance imaging (MRI): advanced radiomic features may compensate for lack of advanced MRI modalities

**Spyridon Bakas,[a,b,c,*,†] Gaurav Shukla,[a,d,†] Hamed Akbari,[a,b,†] Guray Erus,[a,b] Aristeidis Sotiras,[a,b,e,f] Saima Rathore,[a,b] Chiharu Sako,[a,b] Sung Min Ha,[a,b] Martin Rozycki,[a,b] Russell T. Shinohara,[a,g] Michel Bilello,[a,b] and Christos Davatzikos[a,b]**

[a]University of Pennsylvania, Perelman School of Medicine, Center for Biomedical Image Computing and Analytics, Richards Medical Research Laboratories, Philadelphia, PA, United States

[b]University of Pennsylvania, Perelman School of Medicine, Richards Medical Research Laboratories, Department of Radiology, Philadelphia, PA, United States

[c]University of Pennsylvania, Perelman School of Medicine, Richards Medical Research Laboratories, Department of Pathology and Laboratory Medicine, Philadelphia, PA, United States

[d]Thomas Jefferson University, Sidney Kimmel Cancer Center, Department of Radiation Oncology, Philadelphia, PA, United States

[e]Washington University in St. Louis, School of Medicine, Institute for Informatics, Saint Louis, MO, United States

[f]Washington University in St. Louis, Department of Radiology, Saint Louis, MO, United States

[g]University of Pennsylvania, Perelman School of Medicine, Penn Statistics in Imaging and Visualization Center, Department of Biostatistics, Epidemiology, and Informatics, Philadelphia, PA, United States

## Abstract

**Purpose:** Glioblastoma, the most common and aggressive adult brain tumor, is considered noncurative at diagnosis, with 14 to 16 months median survival following treatment. There is increasing evidence that noninvasive integrative analysis of radiomic features can predict overall and progression-free survival, using advanced multiparametric magnetic resonance imaging (Adv-mpMRI). If successfully applicable, such noninvasive markers can considerably influence patient management. However, most patients prior to initiation of therapy typically undergo only basic structural mpMRI (Bas-mpMRI, i.e., T1, T1-Gd, T2, and T2-fluid-attenuated inversion recovery) preoperatively, rather than Adv-mpMRI that provides additional vascularization (dynamic susceptibility contrast-MRI) and cell-density (diffusion tensor imaging) related information.

**Approach:** We assess a retrospective cohort of 101 glioblastoma patients with available Adv-mpMRI from a previous study, which has shown that an initial feature panel (IFP, i.e., intensity, volume, location, and growth model parameters) extracted from Adv-mpMRI can yield accurate overall survival stratification. We focus on demonstrating that equally accurate prediction models can be constructed using augmented radiomic feature panels (ARFPs, i.e., integrating morphology and textural descriptors) extracted solely from widely available Bas-mpMRI, obviating the need for using Adv-mpMRI. We extracted 1612 radiomic features from distinct tumor subregions to build multivariate models that stratified patients as long-, intermediate-, or short-survivors.

**Results:** The classification accuracy of the model utilizing Adv-mpMRI protocols and the IFP was 72.77% and degraded to 60.89% when using only Bas-mpMRI. However, utilizing the ARFP on Bas-mpMRI improved the accuracy to 74.26%. Furthermore, Kaplan–Meier analysis

*Address all correspondence to Spyridon Bakas, E-mail: sbakas@upenn.edu

†These authors contributed equally to this work.

2329-4302/2020/$28.00 © 2020 SPIE

demonstrated superior classification of subjects into short-, intermediate-, and long-survivor classes when using ARFP extracted from Bas-mpMRI.

**Conclusions:** This quantitative evaluation indicates that accurate survival prediction in glioblastoma patients is feasible using solely Bas-mpMRI and integrative advanced radiomic features, which can compensate for the lack of Adv-mpMRI. Our finding holds promise for generalization across multiple institutions that may not have access to Adv-mpMRI and to better inform clinical decision-making about aggressive interventions and clinical trials.

 [DOI: 10.1117/1.JMI.7.3.031505]

**Keywords:** radiomics; glioblastoma; survival; prediction; prognosis; multivariate.

Paper 19292SSRRR received Nov. 15, 2019; accepted for publication May 20, 2020; published online Jun. 9, 2020.

## 1 Introduction

Glioblastoma is the most aggressive malignant primary adult tumor of the central nervous system, with a median survival of 14 to 16 months if standard treatment of surgical resection, chemotherapy, and radiotherapy is followed, and 4 months otherwise.[1] Glioblastomas exhibit highly heterogeneous histological and molecular profiles that are also reflected in their imaging phenotypes[2–4] and in their radiographic appearance, which includes various subregions, i.e., enhancing (ET) and nonenhancing (NET) parts of tumor, as well as the peritumoral brain zone describing edematous and invaded tissue (ED).[5]

There is increasing evidence that quantitative analysis of radiographic (i.e., radiomic) features extracted from multiparametric magnetic resonance imaging (mpMRI) scans can reveal more than just the visually observable cues (i.e., subvisual cues), which can be associated with prediction of clinical outcomes and tumor molecular characteristics.[3,4,6–38] However, most state-of-the-art studies that investigated the predictive value of imaging in comparison with clinical and molecular parameters utilized imaging data obtained from advanced acquisition protocols [advanced multiparametric magnetic resonance imaging (Adv-mpMRI), i.e., T1, T1-Gd, T2, T2-fluid-attenuated inversion recovery (T2-FLAIR), dynamic susceptibility contrast (DSC), and diffusion tensor imaging (DTI)], which are not yet widely incorporated into routine clinical practice except at tertiary/quaternary referral centers of neurosurgical expertise, which constitute the minority of imaging centers where patients present for initial evaluation. This is in part due to limitations of cost, clinical expertise, and/or specialized equipment. Therefore, many of the promising findings may not be easily generalizable or repeatable across institutions.

To address this limitation, this study focused on evaluating the feasibility and performance of predicting the survival of glioblastoma patients using exclusively preoperative baseline basic structural mpMRI (Bas-mpMRI) scans (i.e., T1, T1-Gd, T2, and T2-FLAIR) of the patients, via quantitative integrative analysis of radiomic features. Toward this aim, extensive sets of radiomic features from various glioblastoma subregions (ED, ET, and NET), describing mpMRI signals, were integratively analyzed using multivariate pattern analysis and machine learning methods. Specifically, we evaluate a retrospective cohort of glioblastoma patients from a previous study that has shown accurate prognostic stratification utilizing Adv-mpMRI, and we focus on demonstrating that equally accurate prediction models can be constructed using advanced radiomic features extracted solely from Bas-mpMRI.

## 2 Methods

### 2.1 *Dataset*

A retrospective cohort of 101 patients diagnosed with primary (*de novo*) glioblastoma at the Hospital of the University of Pennsylvania (HUP) between 2006 and 2013 was used in this analysis.[29] The molecular characterization of these tumors was not available, since they were diagnosed prior to the most recent World Health Organization (WHO) classification scheme of

2016, hence they can now be categorized as diffuse astrocytoma not-otherwise-specified, according to the WHO 2016 and the C-IMPACT classification.[39,40] These patients were scanned preoperatively using a standardized Adv-mpMRI acquisition protocol of six different modalities, comprising native (T1) and contrast-enhanced (T1-Gd), T1-weighted, T2-weighted (T2), T2-FLAIR, DTI, and DSC MRI volumes. Mean and median patient age was 62.5 and 61.4 years, respectively (range: 22 to 88.6 years). The protocol was approved by the Institutional Review Board at HUP, and informed consent was obtained from all subjects. No randomization method was used for allocating samples to experimental groups.

Patients were treated with standard maximal safe resection followed by adjuvant chemoradiation using temozolomide and six weeks of daily fractionated radiation, five days per week. The details of this cohort have been described previously,[29] with a median overall survival (OS) of 13 months, consistent with historical series. The described cohort was divided in patients that survived <12 months (short-survivors, $n = 45$) against others, and to patients that survived more than 14 months (long-survivors, $n = 45$) against others. We chose these thresholds based on equal quantiles from the median OS (~13 months) to avoid potential bias toward one of the survival groups (short-survivor versus long-survivor) and while considering that discrimination of groups should be clinically meaningful. The median OS of the described cohorts is not significantly different from the median survival of glioblastoma patients in several randomized phase III trials, noting that our cohort consists of unselected patients rather than those eligible for such trials.[41,42]

## 2.2 *Statistical Consideration for Survival Analysis*

OS was defined as the duration of time between the establishment of diagnosis and the date of death. Mean and median OS was 14.17 and 12.63 months, respectively (range: 0.1 to 68.27, standard deviation: 11.4), and no patient was censored, as all patients have reached the endpoint of death. Kaplan–Meier (KM) curves were generated for the depiction of OS based on the result of each predictive model, as well as for the true classification. The Cox proportional hazards model was used to estimate the hazard ratio of death between groups.[43] Based on our sample size, we are powered to detect predictive performance for a classifier of short-survivors (or, equivalently, long-survivors) with area under the curve (AUC) values of 0.65 or larger with 80% power assuming a 5% type I error rate.

## 2.3 *Equipment and Acquisition Protocol Details*

All the MRI volumes used in this study were acquired in the axial plane using a 3-Tesla Siemens Magnetom Trio A Tim clinical MRI system (Erlangen, Germany), according to the standardized advanced acquisition protocol followed at HUP. The acquired T1 volumes had dimensions of $192 \times 256 \times 192$ pixels, with spatial resolution of $0.976 \times 0.976 \times 1$ mm$^3$, slice spacing of 1 mm, and inversion time (TI), repetition time (TR), and echo time (TE) equal to 950, 1760 and 3.1 ms, respectively. The dimensions of the axial 3-D T1-Gd volumes were $192 \times 256 \times 192$ pixels, with spatial resolution of $0.976 \times 0.976 \times 1$ mm$^3$, slice spacing of 1 mm, and TI, TR, and TE equal to 950, 1760, and 3.1 ms, respectively. The contrast material used in the scans included in this study was either gadodiamide (Omniscan, GE Healthcare, Mickleton, NJ) or gadobenate dimeglumine (MultiHance, Bracco SpA, Milan) and was administered intravenously (IV). The total dose of contrast material was divided into two IV injections to help minimize errors due to potential contrast leakage out of intravascular space. The initial loading dose described the 25% of the total injected contrast material and the second bolus injection the remaining 75%, with a delay of 5 min. The exact contrast material dosage was dependent on patient weight and given on a relative proportion of 0.3 mL/kg. The T2 volumes were acquired prior to any contrast administration, and their dimensions were $208 \times 256 \times 64$ pixels, with spatial resolution of $0.938 \times 0.938 \times 3$ mm$^3$, slice spacing of 3 mm, and TR and TE equal to 4680 and 85 ms, respectively. The T2-FLAIR volumes were acquired between the initial IV injection and the DSC acquisition. The dimensions of the T2-FLAIR images were $192 \times 256 \times 60$ pixels, with spatial resolution of $0.938 \times 0.938 \times 3$ mm$^3$, slice spacing of 3 mm, and TI, TR, and TE equal to 2500, 9420, and 141 ms, respectively. The DSC acquisition was

performed during the second IV injection of the contrast material. The dimensions of the DSC-MRI images were $128 \times 128 \times 20$ pixels, with spatial resolution of $1.72 \times 1.72 \times 3$ mm$^3$, slice spacing of 3 mm, and TR and TE equal to 2000 and 45 ms, respectively. DTI scans [axial two-dimensional (2-D)] were acquired using a single-shot spin echo planar imaging sequence (variant: segmented $k$-space\spoiled, options: partial Fourier-phase\fat saturation), with 95 phase encoding steps. Following acquisition at $b = 0$ s/mm$^2$ (repeated 3 times), diffusion weighted images were acquired ($b = 1000$ s/mm$^2$) with diffusion gradients applied in 30 directions. The dimensions of the DTI volumes were $128 \times 128 \times 40$ pixels (matrix size $= 128 \times 128$, field of view $= 220 \times 220$ mm$^2$), with spatial resolution of $1.72 \times 1.72 \times 3$ mm$^3$, slice spacing of 3 mm, flip angle of 90 deg, imaging frequency of 123, and TR and TE equal to 5000 and 86 ms, respectively.

In this study, we refer to basic-MRI acquisition protocol as the one that comprises T1, T1-Gd, T2, and T2-FLAIR, and to advanced protocol as the one that in addition to the basic protocol includes DSC and DTI volumes.

## 2.4 *Image Preprocessing*

All acquired mpMRI volumes were initially converted to NIfTI,[44] reoriented to the left–posterior–superior coordinate system, and resampled to spatial resolution of $1 \times 1 \times 1$ mm$^3$ by coregistration to the SRI atlas[45] using an affine registration, through the Oxford Center for Functional MRI of the Brain (FMRIB) Linear Image Registration Tool (FLIRT)[46,47] of the FMRIB Software Library (FSL).[48–50] All volumes were then skull stripped using an automated method based on a multiatlas registration and label fusion using a template library of 216 MRI scans and their brain masks.[51] This library was used for target specific template selection and subsequent registrations using a framework of multiatlas segmentation utilizing ensembles,[52] followed by a region-growing step guided by T2, to obtain the final brain mask including the intracranial cerebrospinal fluid (CSF). All mpMRI volumes were then smoothed using a low-level image processing method, namely Smallest Univalue Segment Assimilating Nucleus, in order to reduce high-frequency intensity variations in regions of uniform intensity profile, while preserving the underlying tissue structure.[53] The intensity histograms of all modalities of all patients were matched to the corresponding modality of a single reference patient, who was randomly selected and has an average size tumor when compared to the remaining cohort population. This histogram matching approach was repeated in this study for four different randomly selected patients with an average size tumor (compared to the cohort population) and reproducible results were noted, showing that the final results were not dependent on the selection of a specific reference patient. Furthermore, this histogram matching approach has been notably used routinely in other similar studies.[29,54]

A set of commonly used DTI measures, namely the tensor's fractional anisotropy DTI(FA), radial diffusivity DTI(RAD), axial diffusivity DTI(AX), and apparent diffusion coefficient DTI(ADC), were extracted from the DTI volumes.[55] Furthermore, the DSC-MRI volumes were used to extract maps of the relative cerebral blood volume, peak height, and percentage signal recovery (PSR).[56–58] Hereafter, we treat these DTI measurements and DSC maps as individual imaging volumes.

## 2.5 *Segmentation of Tumor Subregions*

The four modalities of the basic-MRI acquisition protocol (i.e., T1, T1-Gd, T2, and T2-FLAIR) from the preoperative scans of each patient were used to obtain the segmentation labels of the various tumor subregions (Fig. 1). The method used to produce the segmentation labels is called GLISTRboost[59,60] and it defines a hybrid generative-discriminative brain tumor segmentation method. The generative part incorporates a glioma growth model[61–63] and is based on an expectation–maximization framework to segment the brain volumes into tumor (i.e., ET, NET, and ED), as well as healthy tissue labels (i.e., white and gray matter, cerebrospinal fluid, vessels, and cerebellum). During this step, the patient data are coregistered to a standardized atlas coordinate system allowing for estimation of the tumor proportion in various anatomical regions and hence offering location and spatial distribution information. The discriminative

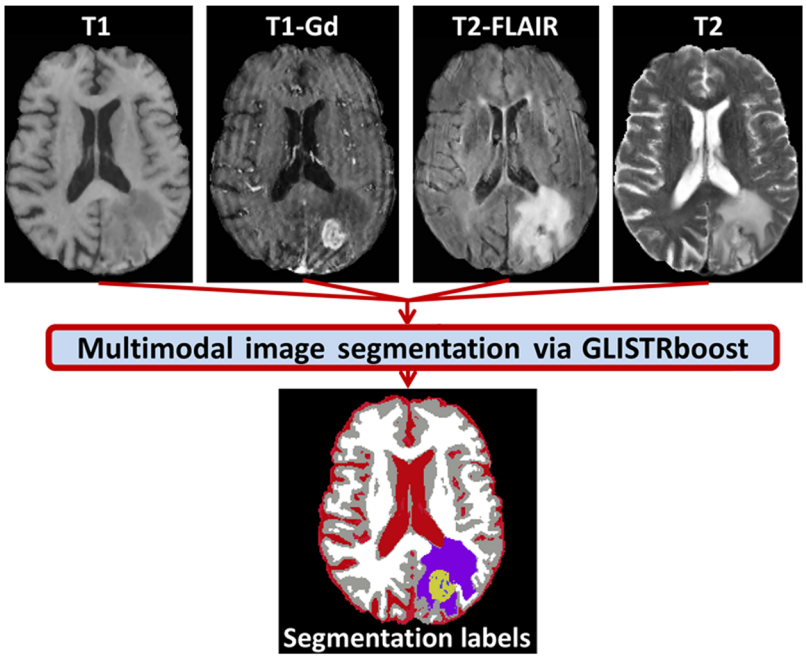


**Fig. 1** Segmentation labels of brain and glioblastoma subregions in multimodal MRI using GLISTRboost.[59,60]

part is based on a gradient boosting[64,65] multiclass classification scheme, which was trained on data provided during the brain tumor segmentation (BraTS) challenge[5,66,67] to refine tumor labels based on information from multiple patients. Finally, a Bayesian strategy[68] is employed to further refine and finalize the tumor segmentation labels based on patient-specific intensity statistics from the four basic modalities available. The derived segmentation labels were considered final after their evaluation and manual revision, when needed, by an expert board-certified neuroradiologist (M. B.).

## 2.6 *Radiomic Features*

### 2.6.1 *Feature extraction*

An extensive panel of 1612 radiomic features was extracted from all the available imaging volumes, based on the segmentation labels of each tumor subregion and while following the image biomarker standardization initiative (IBSI) definitions.[69,70] These features comprised (i) intensity, (ii) volume,[71] (iii) morphology,[72–74] (iv) histogram-based,[29] and (v) textural[75] parameters, including features based on wavelets,[76] gray-level co-occurrence matrix (GLCM),[77] gray-level run-length matrix (GLRLM),[78–81] gray-level size zone matrix (GLSZM),[78–80] and neighborhood gray-tone difference matrix (NGTDM),[82] as well as (vi) spatial information,[83] and (vii) glioma diffusion properties extracted from glioma growth models.[61–63] For the exact feature extraction, we have quantized the image based on the region comprising the union of ET, NET, and ED. The volumetric features were calculated in three dimensions. The textural parameters of GLCM, GLRLM, GLSZM, and NGTDM were extracted based on 16 bins, 27 directions around the center voxel, and a radius of 1 voxel, which defines a neighborhood of $3 \times 3 \times 3$. We note that features (iv), (vi), and (vii) have already shown association with predicting survival when used with Adv-mpMRI acquisition protocol.[29] From this point onward, we refer to the features reported in Ref. 29, comprising (i), (ii), (iv), (vi), and (vii), as initial feature panel (IFP) and the complete set described above as augmented radiomic feature panel. We note that the biological significance of these individual radiomic features remains unknown.

### 2.6.2 *Feature selection*

We hypothesize that the necessary information to conduct this classification task is encapsulated by a subset of all the 1612 features that are used in this study. Therefore, we consider the selection of the most important features as critical, in order to minimize the classification error and eliminate redundancy by removing features with little contribution in the classification. Specifically, a forward-selection framework is used to rank and select a subset of features, based on the classification performance of a support vector machine (SVM). Various subsets of features are assessed by evaluating the contribution of all individual features in the performance of the classifier's accuracy. This feature selection is applied in the complete set of input features using a fivefold cross-validation configuration with convergence criteria of 100 iterations and a tolerance of $10^{-4}$ in the classifier's performance.

## 2.7 *Predictive Modeling*

The problem of modeling the prediction of survival is approached as a binary classification problem, between long-survivor and short-survivor, using a formulation of two multivariate SVM classifiers (SVC) with a linear kernel, similar to Ref. 29. Moreover, after evaluating the similarity of the results obtained using a linear kernel and a radial basis function kernel, we chose the linear kernel for computational simplicity and for generalization purposes. One SVC model is constructed to distinguish between patients that survived <12 months against others (referred to as "short-SVC") and another for discriminating patients that survived more than 14 months against others (referred to as "long-SVC"). The decisions of these classifiers are then combined: (a) patients classified by both classifiers as short-survivors are assigned a label of short-survivors, (b) patients classified by both SVC models as long-survivors are assigned a label of long-survivors, (c) patients classified as long-survivors by the short-SVC and as short-survivors by the long-SVC are given the label of the intermediate survivor, and (d) patients for which the two classifiers disagree (i.e., the short-SVC classified them as short-survivors and the long-SVC as long-survivors) are given a label based on which distance from the two SVM hyperplanes is dominant.

The discrimination of subjects into three groups (short-, intermediate-, and long-survivors) is clinically useful for several reasons. Three-class classification schemes are abundant in oncology. The terminology of "low," "intermediate," and "high" is commonly used in risk assessments, staging systems, and pathological grading systems, for their ease of translation into clinical decision-making. Recommending therapies for patients requires a clinician's assessment of patient performance status and life expectancy, which can be notoriously imprecise; a three-class category of "better than expected," "as expected," and "worse than expected" is practical for routine clinical use, i.e., when trying to customize therapeutic decisions for the patient sitting in front of the physician.

## 2.8 *Cross Validation*

The generalization performance of our predictive modeling was quantitatively validated using a nested fivefold cross validation scheme to provide unbiased performance estimates. In this fivefold configuration, short- and long-survivors have been proportionally and randomly divided into five nonoverlapping smaller equally sized datasets such that they are statistically representative of the whole, and during each fold, four of these subsets were considered to be the discovery/retrospective cohort and 1 as the replication/prospective cohort, which is unseen for this specific fold. During each fold, the replication/prospective cohort is a different subset. This cross-validation (CV) scheme is similar to analyzing the given data as having independent retrospective and prospective cohorts, but in a more statistically robust manner by randomly permuting across the provided data. Furthermore, nested within each of these folds the feature selection was conducted as previously described, and immediately after the feature selection the SVC parameter (c) was optimized on another fivefold CV scheme.

### 2.9 *Code Availability*

The tool used for coregistration of the brain scans (i.e., FLIRT) is publicly available from the FSL, in: fsl.fmrib.ox.ac.uk. The approach used for skull stripping[52] and the segmentation method for preoperative mpMRI brain glioma scans, GLISTRboost,[59,60] has been made available for public use through the Online Image Processing Portal (IPP)[84] of the Center for Biomedical Image Computing and Analytics (CBICA). CBICA's IPP allows users to perform their data analysis using integrated algorithms, without any software installation, while also freely using CBICA's high-performance computing resources. It should be noted that we used the publicly available Python package scikit-learn[85] for the implementation of the gradient boosting algorithm used in GLISTRboost. The Cancer Imaging Phenomics Toolkit (CaPTk),[54,86,87] developed by the CBICA, was used for the (i) seed-point initialization required for GLISTRboost, (ii) denoising approach (SUSAN), as well as (iii) extraction of the radiomic features (i)–(iv) and (vi) described in Sec. 2.6.1. The code source, as well as the executable installer of CaPTk, is available in Ref. 88. The texture features, described in Sec. 2.6.1 as (v), were extracted using the MATLAB® "radiomics" package,[71] written by one of the two equally contributing first authors of the IBSI. The tumor growth parameters [features (vii)] were extracted through the glioma growth model[61–63] incorporated in the generative part of GLISTRboost. Finally, results were originally obtained by G. S. using in-house code written by G. S., S. B., and G. E., with consultation of H. A. These results were subsequently replicated by S. B. and A. S. at two independent sets of experiments.

## 3 Results

### 3.1 *Accuracy Results*

The obtained cross-validated accuracies for classifying glioblastoma patients in short-, intermediate- and long-survivors, when using (a) the Adv-mpMRI and IFP ("IFP advanced" model), (b) the Bas-mpMRI and IFP ("IFP-basic" model), and (c) the Bas-mpMRI and augmented feature panel (AFP) ("AFP-basic" model) were equal to 60,89%, 72.77%, and 74.26%, respectively (Table 1).

We calculated individual performance metrics (sensitivity and specificity) for the individual classifiers (short-SVC and long-SVC) within each model, allowing for a receiver operating characteristic analysis, the interpretation of which should be conducted in pairwise manner (short-SVC and long-SVC) for the three-class classification evaluated in this study (Fig. 2). The classification results from these two classifiers were then combined to build a three-class classifier (short-, intermediate-, and long-survivors), as described in Sec. 2.7. We first evaluated the performance of this three-class classification using the IFP advanced model, similar to our previous work.[29] This model returned an accuracy of 72.77%, which was improved relative to the performance of the individual short-SVC and long-SVC (Tables 1 and 2). We next evaluated the performance of this three-class classification using the IFP-basic model, which resulted in a notable decrement in performance, returning an accuracy of 60.89%. Finally, we utilized the AFP-basic model, which resulted in a classification accuracy of 74.26%.

**Table 1** Accuracy for predicting survival in glioblastoma patients based on various configurations of MRI acquisition protocols and features. IFP and AFP stand for initial and augmented feature panels, respectively.

| Predictive model | MRI acquisition protocol | Features | Accuracy (%) |
|---|---|---|---|
| IFP-advanced | Advanced (basic + DTI + DSC) | IFP | 72.77 |
| IFP-basic | Basic (T1, T1Gd, T2, and T2-FLAIR) | IFP | 60.89 |
| AFP-basic | Basic (T1, T1Gd, T2, and T2-FLAIR) | AFP | 74.26 |

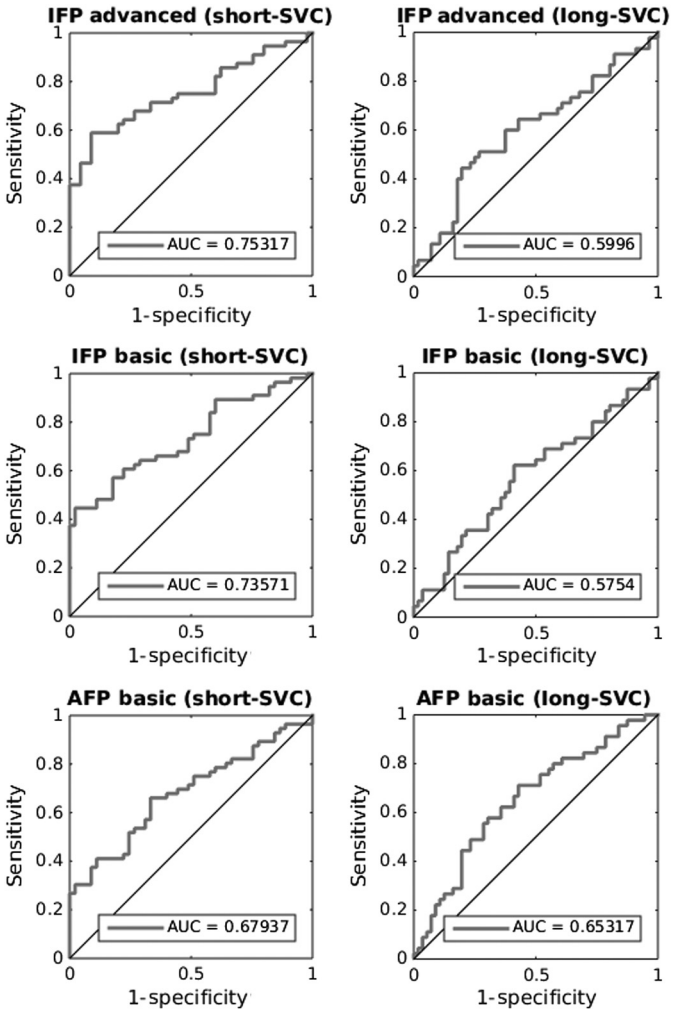


**Fig. 2** ROC analysis for the short-/long-SVCs of each of the predictive models.

**Table 2** Cross-validated performance evaluation metrics for the short-SVC and long-SVC for the three assessed predictive models. IFP and AFP stand for initial and augmented feature panels, respectively.

| | Short-SVC | | | Long-SVC | | |
|---|---|---|---|---|---|---|
| Predictive model | Accuracy (%) | Sensitivity (%) | Specificity (%) | Accuracy (%) | Sensitivity (%) | Specificity (%) |
| IFP-advanced | 66.34 | 55.56 | 75 | 60.39 | 51.11 | 67.86 |
| IFP-basic | 63.37 | 48.89 | 75 | 56.44 | 35.56 | 73.21 |
| AFP-basic | 62.38 | 51.11 | 71.43 | 62.38 | 48.89 | 73.21 |

## 3.2 *Feature Selection*

We analyzed the features selected by the nested fivefold cross validation to determine if the various predictive models actually select features from the varying configurations, as well as to identify which features are selected. Indeed, it is noted that the IFP advanced model selected 69.57% of its features from the basic-MRI protocol and 30.43% from the advanced MRI protocol

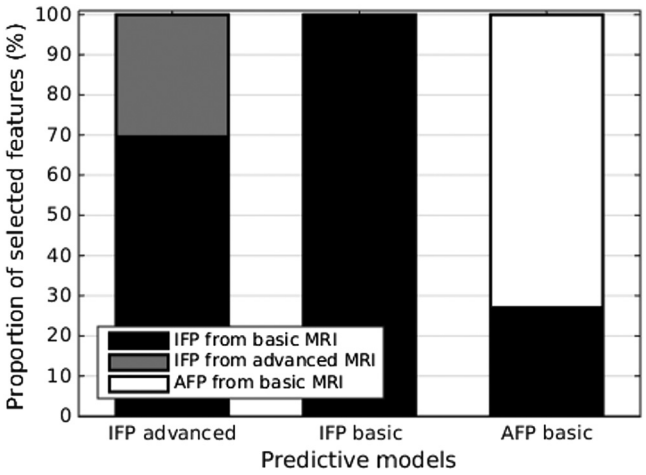


**Fig. 3** Proportion of the selected features for each of the predictive models.

(Fig. 3). Furthermore, the AFP-basic model revealed that 73% of its selected features were obtained from the AFP and the remaining 27% from the IFP (Fig. 3). The list of selected features as well as their type for the IFP advanced and the AFP-basic model are given in Tables 3 and 4 (Appendix), respectively.

### 3.3 *Kaplan–Meier Analysis*

Cox proportional hazard modeling for OS was performed for the classification between short-, intermediate-, and long-survivors based on their real survival classes, as well as on the predictive models. Using the IFP advanced, the median $\pm$ standard deviation OS of the short- and long-survivor groups was $9.1 \pm 7.7$ months and $14.9 \pm 11.3$ months, respectively, and the hazard ratio for death, for short versus long, was 2.02 (95% CI:1.67 to 2.44). Using IFP-basic, the median $\pm$ standard deviation OS of the short- and long-survivor groups was $9.2 \pm 8.8$ months and $14.2 \pm 11.8$ months, respectively; hazard ratio for death was 1.74 (95% CI:1.45 to 2.10). Using the AFP-basic, the median $\pm$ standard deviation OS of the short- and long-survivor groups was $5.1 \pm 3.9$ months and $16.6 \pm 14.8$ months, respectively; hazard ratio for death was 2.84 (95% CI:2.42 to 3.34) (Fig. 4).

## 4 Discussion

Although the widespread adoption of MRI for the diagnosis and management of brain tumors such as glioblastoma has generated large datasets for imaging scientists, the most sophisticated research platforms have been established in affiliation with cancer centers utilizing Adv-mpMRI acquisition protocols, such as DTI and DSC volumes. In prior work, we developed a survival prediction model using radiomic features (described here as IFP) derived from an Adv-mpMRI acquisition protocol.[29] In this work, we demonstrated that a predictive classification model using an AFP, including morphology and texture (radiomic) features, derived only from Bas-mpMRI acquisition protocols, can achieve similar results to models using the IFP derived from Adv-mpMRI acquisition protocols.

We embarked upon this work after noting that many patients referred to our tertiary care institution come with only Bas-mpMRI acquired at those outside hospitals. These patients were not eligible for analysis using the previous prediction model as they lacked DTI and DSC imaging. Furthermore, as we explore multi-institutional validation of these predictive models, we noted that other institutions do not routinely acquire Adv-mpMRI prior to neurosurgical intervention. The goal of generalizing our results to patients from other institutions motivated this work, as we consider prognostic tools as useful only if they can be generalized to all patients. Moreover, as Adv-mpMRI protocols remain limited in their availability, the reach of tools

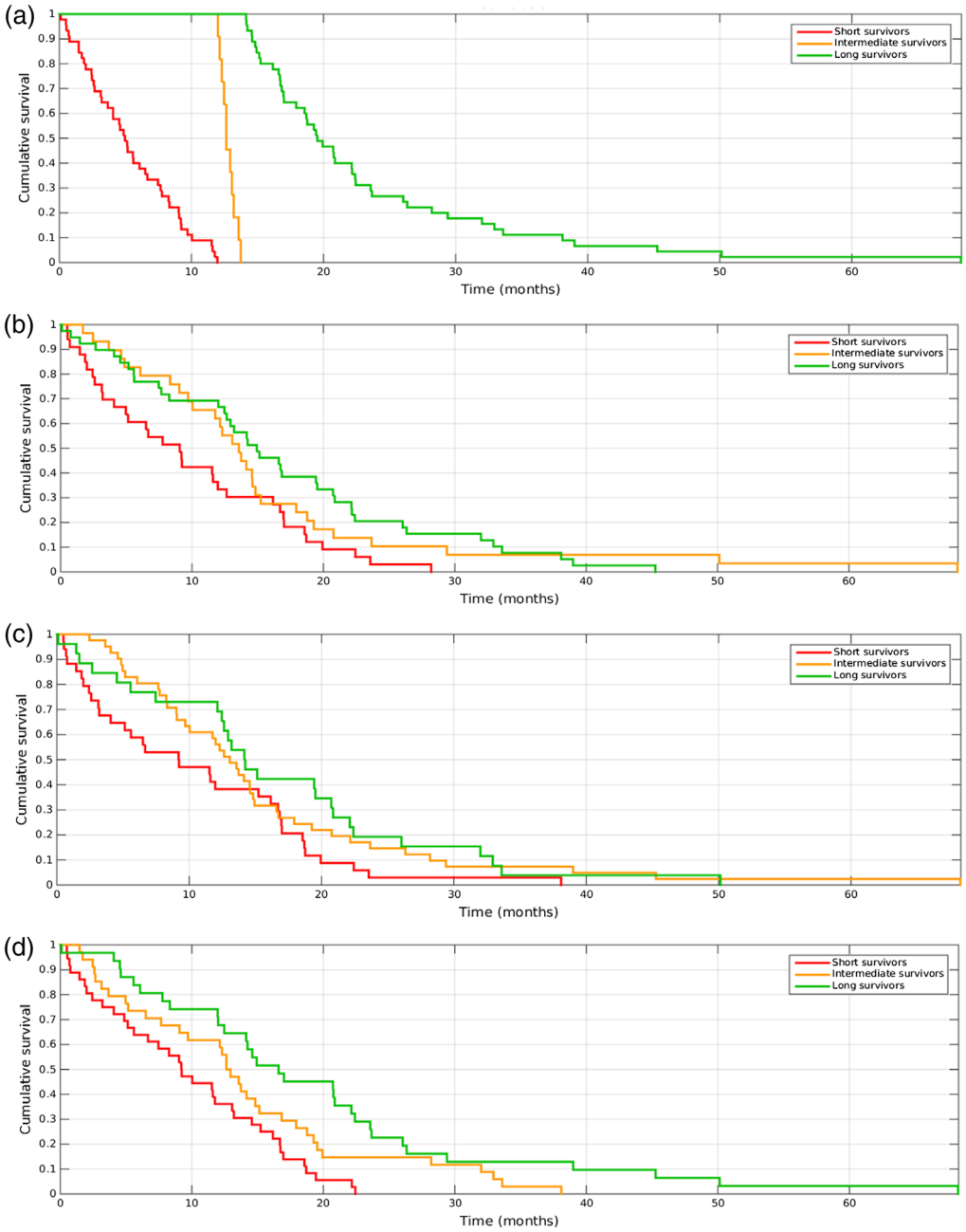


**Fig. 4** KM curves on the provided patient data for their classification on short- (<12 months), intermediate- (between 12 and 14 months), and long-survivors (>14 months), based on (a) the real labels, (b) the IFP-advanced model, (c) the IFP-basic model, and (d) the AFP-basic model.

utilizing those modalities is itself limited. We would, therefore, consider the use of Bas-mpMRI acquisition protocols in the presented predictive models of this study, rendering them as potentially more generalizable/applicable to the majority of glioblastoma patients who undergo such imaging.

We have replicated the results of Ref. 29 in this study using the IFP advanced model, but with different survival thresholds. Unsurprisingly, when we attempted to predict patient survival using only Bas-mpMRI modalities and our IFP (via the IFP-basic model), there was a significant decrement in the performance (Table 1). Importantly, when we expanded the feature set extracted from these basic imaging modalities to incorporate features that may not be visually observable, including statistical texture and morphology features, to build the AFP-basic model, we observed

a significant improvement, yielding the best performance in stratifying patients into long-, intermediate-, and short-survivors (Table 1).

Examination of the receiver operating characteristic (ROC) curves (Fig. 2) and the independent performance evaluation metrics (Table 2) demonstrated that the AFP-basic model was the only one with balanced classification between the classification of short-survivors (short-SVC; <12 months OS) and long-survivors (long-SVC; >14 months OS). This balance is skewed with the IFP-basic or IFP-advanced models, suggesting that the AFP-basic model may be better equipped to handle the classification of short- and long-survivors.

One strength of this work is that we utilize a fivefold cross-validation scheme. We chose this over a 10-fold or leave-one-out scheme, in order to avoid the risk of reporting over-optimistic fitting of the data. Along the same rationale of improved generalizability, we chose a fivefold cross-validation scheme for feature selection, instead of sampling with resubstitution, even though the latter approach yielded even better performance in each classifier. Specifically, the analogous results shown in Table 1 as 74.26%, 72.77%, and 60.89%, for AFP-basic, IFP-advanced, and IFP-basic, respectively, improved to 89.11%, 78.71%, and 75.74%, when we used sampling with resubstitution for the feature selection. It should be noted that the accuracy of prediction by chance (i.e., coin flip) for three-class classification is 33%.

Limitations of this work include the lack of independent prospective evaluation of our method. However, this comprises a future direction. We hope that by demonstrating the feasibility of building successful classifiers from Bas-mpMRI alone, we may elicit collaboration with imaging scientists from other institutions to prospectively validate these findings in multi-institutional datasets. Such validation should facilitate the assessment of (i) the potential effect that acquisition parameter variations can have in downstream radiomic feature analyses, as well as (ii) the harmonized preprocessing prior to any algorithmic application (Sec. 2.4) in mitigating such variations in the protocol settings. Another limitation of this work is the relatively modest classification accuracy. We acknowledge that a classification tool with even higher accuracy could have more immediate clinical utility. At the same time, clinical decision-making for patients with glioblastoma is an inherently uncertain process.

We hypothesize that a model providing a strong survival estimate to patients and clinicians, beyond that achievable with current conventional methods, may provide increased confidence for patients and clinicians making difficult decisions in the context of the uncertainty involved in treating this difficult disease. Furthermore, it may be useful in stratifying/selecting patients for clinical trials, potentially allowing for fewer patients to be needed in order to demonstrate effect of an innovative therapeutic intervention.

## 5 Conclusion

This study has shown evidence of the feasibility of survival prediction in glioblastoma patients using solely Bas-mpMRI, which are more widely available in community settings, and integrative advanced radiomic features, indicating that such features can compensate for the lack of Adv-mpMRI. Further studies including multi-institutional data are required to prove the further generalizability of our findings and evaluate the application of our predictive model to imaging acquisition protocols of current clinical practice in various institutions. This method holds promise to assist clinical decision-making for patients with *de novo* glioblastoma to better select patients for potentially toxic therapies and clinical trials.

## 6 Appendices

Tables 3 and 4 comprise the list of selected features and their type for the 'IFP Advanced' and the 'AFP Basic' models, respectively.

**Table 3** The exact features selected from the IFP-advanced model.

| Type of feature | Description |
|---|---|
| Volumetric | The volume of the complete brain, excluding skull structures |
| Volumetric | The volume of the NET relative to the volume of the ED |
| Spatial | The closest distance of the ED from the ventricles |
| Intensity | The raw average intensity of the ET in the postcontrast T1 (T1-Gd) volume |
| Intensity | The standard deviation of the raw intensities of the ET in the FLAIR volume |
| Intensity | The raw average intensity of the ET in the DTI(AX) map volume |
| Intensity | The raw average intensity of the ET in the DTI(ADC) map volume |
| Histogram-based | 10-binned histogram of the raw intensity values of the ET in the T1-Gd volume (bin 1) |
| Histogram-based | 10-binned histogram of the raw intensity values of the ED in the T1-Gd volume (bin 4) |
| Histogram-based | 10-binned histogram of the raw intensity values of the NET in the T1-Gd volume (bin 2) |
| Histogram-based | 10-binned histogram of the raw intensity values of the ED in the T1 volume (bin 2) |
| Histogram-based | 10-binned histogram of the raw intensity values of the ED in the T2 volume (bin 5) |
| Histogram-based | 10-binned histogram of the raw intensity values of the NET in the FLAIR volume (bin 3) |
| Histogram-based | 10-binned histogram of the raw intensity values of the NET in the FLAIR volume (bin 5) |
| Histogram-based | 10-binned histogram of the raw intensity values of the NET in the FLAIR volume (bin 7) |
| Histogram-based | 10-binned histogram of the raw intensity values of the ED in the DTI(FA) volume (bin 1) |
| Histogram-based | 10-binned histogram of the raw intensity values of the NET in the DTI(RAD) volume (bin 2) |
| Histogram-based | 10-binned histogram of the raw intensity values of the NET in the DTI(RAD) volume (bin 3) |
| Histogram-based | 10-binned histogram of the raw intensity values of the ED in the DSC(PSR) volume (bin 7) |
| Histogram-based | 10-binned histogram of the raw intensity values of the NET in the DSC(PSR) volume (bin 3) |
| Spatial | Percentage of TC volume in the region of the cerebellum |
| Tumor growth model parameter | The estimated diffusion coefficient of white matter, considering all apparent tumors |
| Tumor growth model parameter | The 3-D coordinates (in coronal plane) of the apparent tumor's center of gravity |

**Table 4** The exact features selected from the AFP-basic model.

| Type of feature | Description |
|---|---|
| Volumetric | The volume of the complete brain, excluding skull structures |
| Volumetric | The volume of the ED relative to the volume of the whole tumor |
| Spatial | The closest distance of the TC from the ventricles |
| Intensity | The raw average intensity of the ET in the postcontrast T1 (T1-Gd) volume |

**Table 4** (*Continued*).

| Type of feature | Description |
|---|---|
| Intensity | The standard deviation of the raw intensities of the ET in the T1 volume |
| Histogram-based | Binned histogram of the raw intensity values of the ED in the T1 volume (bin 2) |
| Histogram-based | Binned histogram of the raw intensity values of the ED in the FLAIR volume (bin 2) |
| Histogram-based | Binned histogram of the raw intensity values of the NET in the FLAIR volume (bin 1) |
| Spatial | Percentage of TC volume in the occipital lobe |
| Spatial | Percentage of TC volume in the region of brain stem |
| Volumetric | Eccentricity metric for NET: sqrt$[1 - a * b/c2]$, where $c$ is the longest semiprincipal axes of an ellipsoid fitted on the NET, and $a$ and $b$ are the second and third longest semiprincipal axes of the ellipsoid |
| Textural (GLCM) | The energy within the ET in the T1-Gd volume, considering 26-connected neighboring voxels in the 3-D volume |
| Textural (GLCM) | The entropy within the ET in the T1-Gd volume, considering 26-connected neighboring voxels in the 3-D volume |
| Textural (GLCM) | The variance within the ET in the T1-Gd volume, considering 26-connected neighboring voxels in the 3-D volume |
| Textural (GLCM) | The autocorrelation within the ET in the T1-Gd volume, considering 26-connected neighboring voxels in the 3-D volume |
| Textural (GLCM) | The energy within the ET in the T1 volume, considering 26-connected neighboring voxels in the 3-D volume |
| Textural (GLCM) | The contrast within the ET in the T1 volume, considering 26-connected neighboring voxels in the 3-D volume |
| Textural (GLCM) | The contrast within the ED in the T1-Gd volume, considering 26-connected neighboring voxels in the 3-D volume |
| Textural (GLCM) | The SumAverage within the ED in the T1-Gd volume, considering 26-connected neighboring voxels in the 3-D volume |
| Textural (GLCM) | The contrast within the ED in the T2 volume, considering 26-connected neighboring voxels in the 3-D volume |
| Textural (GLCM) | The contrast within the NET in the T1-Gd volume, considering 26-connected neighboring voxels in the 3-D volume |
| Textural (GLCM) | The energy within the NET in the T1 volume, considering 26-connected neighboring voxels in the 3-D volume |
| Textural (GLCM) | The variance within the NET in the T1 volume, considering 26-connected neighboring voxels in the 3-D volume |
| Textural (GLCM) | The correlation within the NET in the T2 volume, considering 26-connected neighboring voxels in the 3-D volume |
| Textural (GLCM) | The variance within the NET in the T2 volume, considering 26-connected neighboring voxels in the 3-D volume |
| Textural (GLRLM) | The "gray-level variance" within the ET in the T1-Gd volume, considering the 13 main directions in the 3-D volume |
| Textural (GLRLM) | The "run-length variance" within the ET in the T2 volume, considering the 13 main directions in the 3-D volume |
| Textural (GLRLM) | The "run-length variance" within the ED in the T1 volume, considering the 13 main directions in the 3-D volume |

**Table 4** (*Continued*).

| Type of feature | Description |
|---|---|
| Textural (GLSZM) | The "low-gray-level zone emphasis" within the ET in the T2 volume, while zones of different sizes are computed using a 26-voxel connectivity |
| Textural (GLSZM) | The "small zone low-gray-level emphasis" within the ED in the T1 volume, while zones of different sizes are computed using a 26-voxel connectivity |
| Textural (GLSZM) | The "low-gray-level zone emphasis" within the ED in the T2 volume, while zones of different sizes are computed using a 26-voxel connectivity |
| Textural (GLSZM) | The "gray-level variance" within the ED in the FLAIR volume, while zones of different sizes are computed using a 26-voxel connectivity |
| Textural (GLSZM) | The "high-gray-level zone emphasis" within the NET in the FLAIR volume, while zones of different sizes are computed using a 26-voxel connectivity |
| Textural (NGTDM) | The strength within the ET in the T1-Gd volume, considering a 26-voxel connectivity |
| Textural (NGTDM) | The busyness within the ET in the T2 volume, considering a 26-voxel connectivity |
| Textural (NGTDM) | The busyness within the ED in the FLAIR volume, considering a 26-voxel connectivity |
| Textural (NGTDM) | The contrast within the NET in the T2 volume, considering a 26-voxel connectivity |

## Disclosures

The authors have no relevant financial interests in the manuscript and no other potential conflicts of interest to disclose.

## Acknowledgments

This work was partly supported by grants awarded from the National Institutes of Health (NIH) under Award Nos. NIH/NINDS R01NS042645 and NIH/NCI/ITCR U24CA189523. The content is solely the responsibility of the authors and does not necessarily represent the official views of the NIH.

## References

1. D. R. Johnson and B. P. O'Neill, "Glioblastoma survival in the United States before and during the temozolomide era," *J. Neuro Oncol.* **107**(2), 359–364 (2011).
2. S. Rathore et al., "Imaging pattern analysis reveals three distinct phenotypic subtypes of GBM with different survival rates," *Neuro Oncol.* **18**(Suppl.6), vi128 (2016).
3. H. J. Aerts et al., "Decoding tumour phenotype by noninvasive imaging using a quantitative radiomics approach," *Nat. Commun.* **5**, 4006 (2014).
4. H. Itakura et al., "Magnetic resonance image features identify glioblastoma phenotypic subtypes with distinct molecular pathway activities," *Sci. Transl. Med.* **7**(303), 303ra138–303ra138 (2015).
5. B. H. Menze et al., "The multimodal brain tumor image segmentation benchmark (BRATS)," *IEEE Trans. Med. Imaging* **34**(10), 1993–2024 (2015).
6. D. Assefa et al., "Robust texture features for response monitoring of glioblastoma multiforme on T1-weighted and T2-FLAIR MR images: a preliminary investigation in terms of identification and segmentation," *Med. Phys.* **37**(4), 1722–1736 (2010).
7. H. L. Aerts, "The potential of radiomic-based phenotyping in precision medicine: a review," *JAMA Oncol.* **2**(12), 1636–1642 (2016).
8. V. Kumar et al., "Radiomics: the process and the challenges," *Magn. Reson. Imaging* **30**(9), 1234–1248 (2012).

9. P. Lambin et al., "Radiomics: extracting more information from medical images using advanced feature analysis," *Eur. J. Cancer* **48**(4), 441–446 (2012).
10. R. J. Gillies, P. E. Kinahan, and H. Hricak, "Radiomics: images are more than pictures, they are data," *Radiology* **278**(2), 563–577 (2015).
11. L. S. Hu et al., "Multi-parametric MRI and texture analysis to visualize spatial histologic heterogeneity and tumor extent in glioblastoma," *PLoS One* **10**(11), e0141506 (2015).
12. A. M. Rutman and M. D. Kuo, "Radiogenomics: creating a link between molecular diagnostics and diagnostic imaging," *Eur. J. Radiol.* **70**(2), 232–241 (2009).
13. C. C. Jaffe, "Imaging and genomics: is there a synergy?" *Radiology* **264**(2), 329–331 (2012).
14. C. Proud, "Radiogenomics: the promise of personalized treatment in radiation oncology?" *Clin. J. Oncol. Nurs.* **18**(2), 185 (2014).
15. B. S. Rosenstein et al., "Radiogenomics: radiobiology enters the era of big data and team science," *Int. J. Radiat. Oncol. Biol. Phys.* **89**(4), 709–713 (2014).
16. B. M. Ellingson, "Radiogenomics and imaging phenotypes in glioblastoma: novel observations and correlation with molecular characteristics," *Curr. Neurol Neurosci. Rep.* **15**(1), 506 (2015).
17. A. Mahajan et al., "Radiogenomics of glioblastoma: a window into its imaging and molecular variability," *Cancer Imaging* **15**(Suppl 1), P14 (2015).
18. M. A. Mazurowski, "Radiogenomics: what it is and why it is important," *J. Am. Coll. Radiol.* **12**(8), 862–866 (2015).
19. E. S. Tykocinski et al., "Use of magnetic perfusion-weighted imaging to determine epidermal growth factor receptor variant III expression in glioblastoma.," *Neuro Oncol.* **14**(5), 613–623 (2012).
20. O. Gevaert et al., "Abstract 5561: radiogenomic analysis indicates MR images are potentially predictive of EGFR mutation status in glioblastoma multiforme," in *Proc. 103rd Annu. Meeting Am. Assoc. for Cancer Res.* (2012).
21. O. Gevaert et al., "Glioblastoma multiforme: exploratory radiogenomic analysis by using quantitative image features," *Radiology* **273**(1), 168–174 (2014).
22. D. A. Gutman et al., "MR imaging predictors of molecular profile and survival: multi-institutional study of the TCGA glioblastoma data set," *Radiology* **267**(2), 560–569 (2013).
23. M. A. Mazurowski, A. Desjardins, and J. M. Malof, "Imaging descriptors improve the predictive power of survival models for glioblastoma patients," *Neuro Oncol.* **15**(10), 1389–1394 (2013).
24. H. Akbari et al., "Imaging surrogates of infiltration obtained via multiparametric imaging pattern analysis predict subsequent location of recurrence of glioblastoma," *Neurosurgery* **78**(4), 572–580 (2016).
25. H. Akbari et al., "Pattern analysis of dynamic susceptibility contrast-enhanced MR imaging demonstrates peritumoral tissue heterogeneity," *Radiology* **273**(2), 502–510 (2014).
26. S. Bakas et al., "Highly-expressed wild-type EGFR and EGFRvIII mutant glioblastomas have similar MRI signature, consistent with deep peritumoral infiltration," *Neuro Oncol.* **18**(Suppl.6), vi125 (2016).
27. A. Fathi Kazerooni et al., "Imaging signatures of glioblastoma molecular characteristics: a radiogenomics review," *J. Magn. Reson. Imaging* (2019).
28. Z. A. Binder et al., "Extracellular EGFR289 activating mutations confer poorer survival and exhibit radiographic signature of enhanced motility in primary glioblastoma," *Neuro Oncol.* **18**(Suppl.6), vi105–vi106 (2016).
29. L. Macyszyn et al., "Imaging patterns predict patient survival and molecular subtype in glioblastoma via machine learning techniques," *Neuro Oncol.* **18**(3), 417–425 (2016).
30. B. J. Gill et al., "MRI-localized biopsies reveal subtype-specific differences in molecular and cellular composition at the margins of glioblastoma.," *Proc. Natl. Acad. Sci. U. S. A.* **111**(34), 12550–12555 (2014).
31. R. Jain et al., "Outcome prediction in patients with glioblastoma by using imaging, clinical, and genomic biomarkers: focus on the nonenhancing component of the tumor," *Radiology* **272**(2), 484–493 (2014).

32. J. Arevalo-Perez et al., "T1-weighted dynamic contrast-enhanced MRI as a noninvasive biomarker of epidermal growth factor receptor vIII status," *Am. J. Neuroradiol* **36**(12), 2256–2261 (2015).
33. D. Bonekamp et al., "Association of overall survival in patients with newly diagnosed glioblastoma with contrast-enhanced perfusion MRI: comparison of intraindividually matched T1- and T2*-based bolus techniques," *J. Magn. Reson. Imaging* **42**(1), 87–96 (2015).
34. M. Nicolasjilwan et al., "Addition of MR imaging features and genetic biomarkers strengthens glioblastoma survival prediction in TCGA patients," *J. Neuroradiol.* **42**(4), 212–221 (2015).
35. N. Batmanghelich et al., "Probabilistic modeling of imaging, genetics and diagnosis," *IEEE Trans. Med. Imaging* **35**, 1765–1779 (2016).
36. E. Rios Velazquez et al., "Fully automatic GBM segmentation in the TCGA-GBM dataset: prognosis and correlation with VASARI features," *Sci. Rep.* **5**, 16822 (2015).
37. S. Burth et al., "Clinical parameters outweigh diffusion- and perfusion-derived MRI parameters in predicting survival in newly diagnosed glioblastoma," *Neuro Oncol.* **18**(12), 1673–1679 (2016).
38. S. Bakas et al., "In vivo detection of EGFRvIII in glioblastoma via perfusion magnetic resonance imaging signature consistent with deep peritumoral infiltration: the $\varphi$-index," *Clin. Cancer Res.* **23**(16), 4724–4734 (2017).
39. D. N. Louis et al., "cIMPACT-NOW: a practical summary of diagnostic points from round 1 updates," *Brain Pathol.* **29**(4), 469–472 (2019).
40. D. N. Louis et al., "The 2016 World Health Organization classification of tumors of the central nervous system: a summary," *Acta Neuropathol.* **131**(6), 803–820 (2016).
41. R. Stupp et al., "Effects of radiotherapy with concomitant and adjuvant temozolomide versus radiotherapy alone on survival in glioblastoma in a randomised phase III study: 5-year analysis of the EORTC-NCIC trial," *Lancet Oncol.* **10**(5), 459–466 (2009).
42. M. R. Gilbert et al., "Dose-dense temozolomide for newly diagnosed glioblastoma: a randomized phase III clinical trial," *J. Clin. Oncol.* **31**(32), 4085–4091 (2013).
43. D. R. Cox, "Regression models and life-tables," in *Breakthroughs in Statistics: Methodology and Distribution*, S. Kotz and N. L. Johnson, Eds., pp. 527–541, Springer, New York (1992).
44. R. W. Cox et al., "A (sort of) new image data format standard: {NIfTI-1}," in *Tenth Annu. Meeting of the Organ. for Hum. Brain Mapp.* (2004).
45. T. Rohlfing et al., "The SRI24 multi-channel atlas of normal adult human brain structure," *Hum. Brain Mapp.* **31**, 798–819 (2010).
46. M. Jenkinson and S. Smith, "A global optimisation method for robust affine registration of brain images," *Med. Image Anal.* **5**(2), 143–156 (2001).
47. M. Jenkinson et al., "Improved optimization for the robust and accurate linear registration and motion correction of brain images," *NeuroImage* **17**(2), 825–841 (2002).
48. M. Jenkinson et al., "FSL," *NeuroImage* **62**, 782–790 (2012).
49. S. M. Smith et al., "Advances in functional and structural MR image analysis and implementation as FSL," *NeuroImage* **23**(Suppl. 1), S208–S219 (2004).
50. M. W. Woolrich et al., "Bayesian analysis of neuroimaging data in FSL," *NeuroImage* **45**(1), S173–S186 (2009).
51. J. Doshi et al., "Multi-atlas skull-stripping," *Acad. Radiol.* **20**, 1566–1576 (2013).
52. J. Doshi et al., "MUSE: MUlti-atlas region segmentation utilizing ensembles of registration algorithms and parameters, and locally optimal atlas selection," *NeuroImage* **127**, 186–195 (2016).
53. S. M. Smith and J. M. Brady, "SUSAN—a new approach to low level image processing," *Int. J. Comput. Vision* **23**(1), 45–78 (1997).
54. C. Davatzikos et al., "Cancer Imaging Phenomics Toolkit: quantitative imaging analytics for precision diagnostics and predictive modeling of clinical outcome," *J. Med. Imaging* **5**(1), 011018 (2018).
55. J. Soares et al., "A hitchhiker's guide to diffusion tensor imaging," *Front. Neurosci.* **7**(31), (2013).

56. J. L. Boxerman, K. M. Schmainda, and R. M. Weisskoff, "Relative cerebral blood volume maps corrected for contrast agent extravasation significantly correlate with glioma tumor grade, whereas uncorrected maps do not," *Am. J. Neuroradiol.* **27**(4), 859–867 (2006).
57. R. Mangla et al., "Percentage signal recovery derived from MR dynamic susceptibility contrast imaging is useful to differentiate common enhancing malignant lesions of the brain," *Am. J. Neuroradiol.* **32**(6), 1004–1010 (2011).
58. S. Cha et al., "Differentiation of glioblastoma multiforme and single brain metastasis by peak height and percentage of signal intensity recovery derived from dynamic susceptibility-weighted contrast-enhanced perfusion MR imaging," *Am. J. Neuroradiol.* **28**(6), 1078–1084 (2007).
59. S. Bakas et al., "GLISTRboost: combining multimodal MRI segmentation, registration, and biophysical tumor growth modeling with gradient boosting machines for glioma segmentation," *Brainlesion: Glioma, Mult. Scler. Stroke Traumatic Brain Injuries* **9556**, 144–155 (2016).
60. K. Zeng et al., "Segmentation of gliomas in pre-operative and post-operative multimodal magnetic resonance imaging volumes based on a hybrid generative-discriminative framework," *Brainlesion: Glioma, Mult. Scler. Stroke Traumatic Brain Injuries* **10154**, 184–194 (2017).
61. C. Hogea et al., "A robust framework for soft tissue simulations with application to modeling brain tumor mass effect in 3D MR images," *Phys. Med. Biol.* **52**(23), 6893 (2007).
62. C. Hogea, C. Davatzikos, and G. Biros, "Brain-tumor interaction biophysical models for medical image registration," *SIAM J. Sci. Comput.* **30**(6), 3050–3072 (2008).
63. C. Hogea, C. Davatzikos, and G. Biros, "An image-driven parameter estimation problem for a reaction–diffusion glioma growth model with mass effects," *J. Math. Biol.* **56**(6), 793–825 (2008).
64. J. H. Friedman, "Greedy function approximation: a gradient boosting machine," *Ann. Stat.* **29**, 1189–1232 (2001).
65. J. H. Friedman, "Stochastic gradient boosting," *Comput. Stat. Data Anal.* **38**(4), 367–378 (2002).
66. S. Bakas et al., "Advancing the cancer genome atlas glioma MRI collections with expert segmentation labels and radiomic features," *Nat. Sci. Data* **4**, 170117 (2017).
67. S. Bakas et al., "Identifying the best machine learning algorithms for brain tumor segmentation, progression assessment, and overall survival prediction in the BRATS challenge," https://arxiv.org/abs/1811.02629 (2018).
68. S. Bakas et al., "Fast semi-automatic segmentation of focal liver lesions in contrast-enhanced ultrasound, based on a probabilistic model," *TCIV Comput. Methods Biomech. Biomed. Eng.: Imaging Vis.* **5**(5), 329–338 (2017).
69. A. Zwanenburg et al., "Image biomarker standardisation initiative," ArXiv e-prints, https://arxiv.org/abs/1612.07003 (2016).
70. A. Zwanenburg et al., "The image biomarker standardization initiative: standardized quantitative radiomics for high-throughput image-based phenotyping," *Radiology* **295**, 191145.
71. M. Vallières et al., "A radiomics model from joint FDG-PET and MRI texture features for the prediction of lung metastases in soft-tissue sarcomas of the extremities," *Phys. Med. Biol.* **60**(14), 5471 (2015).
72. J. Max, "Quantizing for minimum distortion," *IRE Trans. Inf. Theory* **6**(1), 7–12 (1960).
73. S. Lloyd, "Least squares quantization in PCM," *IEEE Trans. Inf. Theory* **28**(2), 129–137 (1982).
74. Q. Li and J. G. Griffiths, "Least squares ellipsoid specific fitting," in *Proc. Geom. Model. Process.*, pp. 335–340 (2004).
75. G. Thibault et al., "Shape and texture indexes application to cell nuclei classification," *Int. J. Pattern Recognit. Artif. Intell.* **27**(01), 1357002 (2013).
76. G. Collewet, M. Strzelecki, and F. Mariette, "Influence of MRI acquisition protocols and image intensity normalization methods on texture classification," *Magn. Reson. Imaging* **22**(1), 81–91 (2004).
77. R. M. Haralick, K. Shanmugam, and I. Dinstein, "Textural features for image classification," *IEEE Trans. Syst. Man Cybern.* **SMC-3(6)**, 610–621 (1973).

78. M. M. Galloway, "Texture analysis using gray level run lengths," *Comput. Graphics Image Process.* **4**(2), 172–179 (1975).
79. A. Chu, C. M. Sehgal, and J. F. Greenleaf, "Use of gray value distribution of run lengths for texture analysis," *Pattern Recognit. Lett.* **11**(6), 415–419 (1990).
80. B. V. Dasarathy and E. B. Holder, "Image characterizations based on joint gray level—run length distributions," *Pattern Recognit. Lett.* **12**(8), 497–502 (1991).
81. X. Tang, "Texture information in run-length matrices," *IEEE Trans. Image Process.* **7**(11), 1602–1609 (1998).
82. M. Amadasun and R. King, "Textural features corresponding to textural properties," *IEEE Trans. Syst. Man Cybern.* **19**(5), 1264–1274 (1989).
83. M. Bilello et al., "Population-based MRI atlases of spatial distribution are specific to patient and tumor characteristics in glioblastoma," *NeuroImage: Clin.* **12**, 34–40 (2016).
84. www.ipp.cbica.upenn.edu
85. F. Pedregosa et al., "Scikit-learn: machine learning in Python," *J. Mach. Learn. Res.* **12**(Oct), 2825–2830 (2011).
86. S. Pati et al., "Cancer and Phenomics Toolkit (CAPTk): a software suite for computational oncology and radiomics," in *Radiol. Soc. North Am. 2016 Sci. Assembly and Annu. Meeting*, Chicago, Illinois (2016).
87. S. Rathore et al., "Brain Cancer Imaging Phenomics Toolkit (brain-CaPTk): an interactive platform for quantitative analysis of glioblastoma," *Brainlesion* **10670**, 133–145 (2018).
88. www.cbica.upenn.edu/captk.

**Spyridon Bakas** received his BSc degree in computer science from Kingston University, London, in 2006, his MSc degree in vision, imaging and virtual environments from University College London, 2007, and his PhD in medical image computing and analysis from Kingston University in 2014. Since then he is with the Center for Biomedical Image Computing and Analytics (CBICA) at the University of Pennsylvania, Philadelphia, Pennsylvania, USA focusing on developing advanced computational algorithms for addressing clinical requirements.

**Gaurav Shukla**, MD, PhD, is a board-certified radiation oncologist, who sees patients in the Christiana Care Health System, with expertise in stereotactic radiosurgery, prostate brachytherapy, and other advanced radiation therapy techniques. He is also an adjunct research assistant professor of Radiology and Radiation Oncology at the University of Pennsylvania, where he collaborates with other experts to develop image-based personalized medicine approaches for patients with cancer.

**Hamed Akbari** received his PhD in Mechano-Micro Engineering with focus on artificial neural networks in robotic surgery from the Tokyo Institute of Technology after obtaining his MD from the medical school at the Tehran University of Medical Sciences. Over the past several years, his research efforts have focused on medical image processing, medical artificial intelligence, personalized/precision medicine, and technologies for minimally invasive procedures.

Biographies of the other authors are not available.